

1 A search for highly ionizing, short tracks at the CMS detector

In this chapter a search for highly ionizing, short tracks is presented. The chapter will be structured as follows: In Section 1.1 a motivation will be given, followed by an overview of the general search strategy in Section 1.2. As the variable dE/dx plays a crucial role in this analysis, a general introduction and different possible parametrizations will be introduced in Section 1.3. In this context also the conducted offline calibration of the silicon pixel detector will be explained. After presenting the simulated SM and signal samples which were used in this analysis (Section 1.4) the event selection is shown (Section 1.5). Then, the various sources of background are characterized (Section ??) and the methods to estimate their size are presented (1.6). As a final step an optimization in the search sensitivity is done, which can be found in Section 1.7. The chapter concludes by presenting the results of this analysis in Section 1.9, and after a short introduction to the statistical methods of limit setting (Section 1.8), the results will be interpreted in the context of Supersymmetry (Section 1.10).

1.1 Motivation

As it was already pointed out in Chapter ??, Supersymmetry is able to offer solutions to unexplained phenomena in astrophysics and can solve the shortcomings of the Standard Model of particle physics. Unfortunately, due to the unknown mechanism of supersymmetry breaking, the most general parametrization of Supersymmetry introduces over 100 new dimensions which opens up an incredibly huge phenomenologically rich space, leading to very different possible signature at particle colliders. During the Phase I run at the LHC in 2012, a variety of different searches, optimized on the hunt for supersymmetry were conducted. At the CMS and at the ATLAS experiments, taking data from proton-proton collisions, a strong focus was put on the search for hints of SUSY in the strong production sector (e.g. [1–3]). This led already to a wide exclusion in SUSY space, which nevertheless still offers some very interesting non-excluded parameter regions. The search for SUSY in more "exotic" regions gains therefore more and more attention. Typical SUSY scenarios which are not easily excluded by the general SUSY searches consists of so-called compressed spectra, where two or more particles are nearly degenerate in their masses. When mother and daughter particles are almost mass-degenerate, the remaining decay product in a two body decay can be very soft in p_T , making those scenarios very challenging to search for. Thus supersymmetric scenarios with compressed spectra are usually much weaker constrained.

One possible scenario in R-parity conserved Supersymmetry is where the lightest neutralino (χ_1^0) is almost mass-degenerate with the lightest chargino (χ_1^\pm). Such a mass-degeneracy naturally occurs in case of a wino-like neutralinos and charginos, as the mass gap is fully determined by higher loop correction as explained in Section ??. SUSY models with a wino-like lightest neutralino are especially interesting because they are able to

explain the sources of the relic density. Although such a model is not able to make up the full relic density thermally produced for $m_{\tilde{\chi}_1^0} \lesssim 2.9$ TeV from the lightest neutralino [4], it can still be the dominant part when it is non-thermally produced via the decay of a long-lived particle [5]. A very good candidate for the long-lived particle is hence the wino-like chargino.

A chargino can be produced via chargino pair production through a photon or a Z boson exchange. The chargino decays then via a virtual W boson to the lightest neutralino and fermion-fermion pair (e.g. a pion). This process is illustrated in the Feynman diagram shown in Fig. 1.1.

Other possible production channels are the exchange of a supersymmetric Higgs boson or via a t-channel squark exchange. The corresponding Feynman diagrams for the tree level production channels are shown in Fig. 1.2.

Another possibility of chargino production is the chargino neutralino production channel. On tree level, there exist two production mechanism: the s-channel W boson exchange and the t-channel squark exchange. See Fig. 1.3 for the Feynman diagrams.

Even if a supersymmetric model with nearly mass-degenerate $\tilde{\chi}_1^\pm$ and $\tilde{\chi}_1^0$ leads to more exotic signatures at the CMS experiment, there have been already several analyses conducted in CMS which are in principle (even not all were designed to be) sensitive to these models. Among those are a search for long-lived charged particles [6], which was mainly designed for particles which have such a long lifetime that they travel through the full detector without decaying and a search for disappearing tracks [7] which looked for rather intermediate lifetimes, where the charginos decays already inside the tracker. Within [7], a study was done, based on an interpretation exercise [8] within the phenomenological MSSM (see Section ?? for a detailed introduction to the pMSSM), which tests the exclusion power for various analyses done at CMS. Figure 1.4 shows the number of excluded pMSSM space points at 95% C.L. and the fraction of excluded points as a function of the chargino lifetime for the following analyses: The search for long-lived charges particles [6] (red area), the search for disappearing tracks [7] (purple area), and a collection of

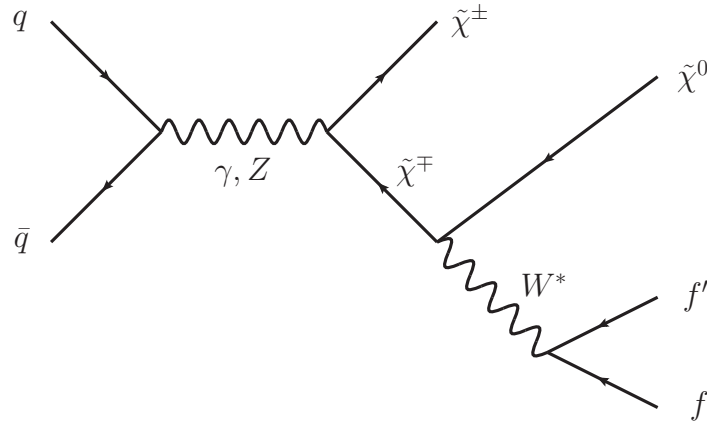


Figure 1.1: Feynman diagram showing a possible production mechanism of a chargino pair and the decay channel of a chargino.

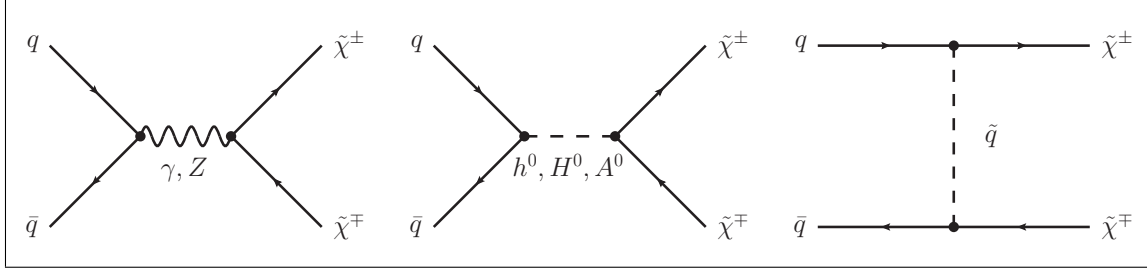


Figure 1.2: Main tree level diagrams for chargino pair production.

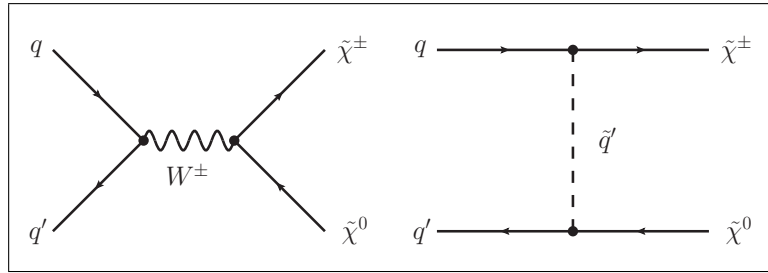


Figure 1.3: Main tree level diagrams for chargino neutralino production.

many general SUSY searches at CMS [10] (blue area). The black line indicates the unexcluded pMSSM parameter points. The sampling of the parameter space points was done according to a prior probability density function which takes pre-LHC data and results from indirect SUSY searches into account (see [8] for further details). In the lower part of Fig. 1.4, it can be seen that the general SUSY searches are mostly sensitive to shorter chargino lifetimes ($c\tau \lesssim 10 \text{ cm}$)¹ whereas the search for disappearing tracks is sensitive on supersymmetric models with chargino lifetimes between $35 \text{ cm} \lesssim c\tau \lesssim 100 \text{ cm}$.

This analysis is targeting the gap between the disappearing track search (purple area) and the searches which are sensitive to instantaneously decaying charginos (blue area). The idea is to make use of the variable dE/dx which can be very discriminating for particles with high mass. The challenges of such a search and the general strategy of this analysis will be presented in the next section.

1.2 General search strategy

When searching for supersymmetric models with long-lived $\tilde{\chi}_1^\pm$, the strategy is of course highly dependent on the actual lifetime of the chargino. For long lifetimes, the chargino can reach the muon chambers and can be reconstructed as a muon (even with a longer time-of-flight). For lower lifetimes, the chargino can already decay inside the detector (e.g. the tracker), hence cannot be reconstructed as a muon, but leads only to an isolated track in the tracker. The detector signatures of these two scenarios are visualised in Fig. 1.5, where in a cross-sectional view of the CMS detector simulated chargino-chargino events

¹It should be mentioned, that the interpretation exercise relied on the use of fast simulation techniques which are not capable of simulating charginos with lifetimes $c\tau > 1 \text{ cm}$. It could therefore not be tested to which exact upper lifetime the searches combined in the blue area are sensitive to.

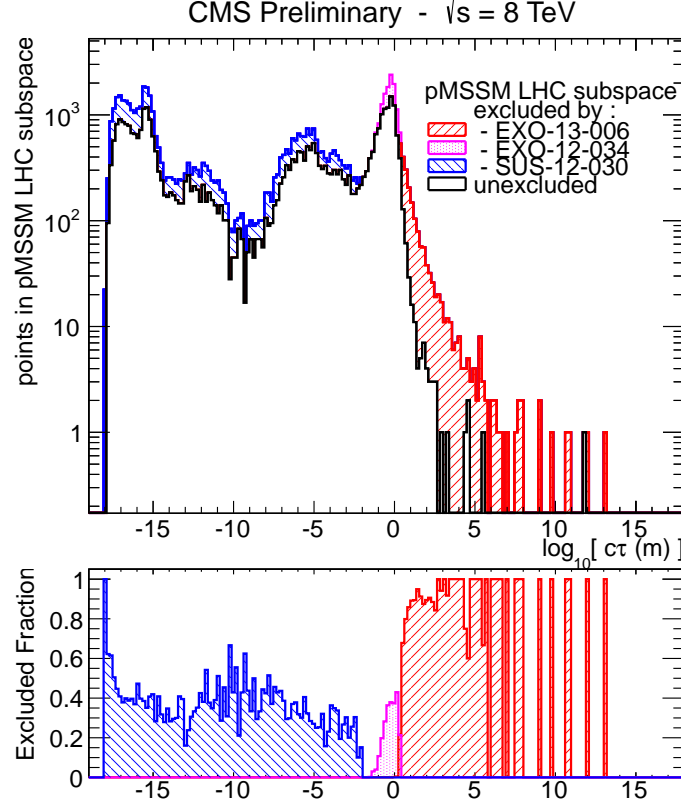


Figure 1.4: The number of excluded pMSSM space points at 95% C.L. and the fraction of excluded pMSSM space points (bottom part) vs. the chargino lifetime. Taken from: [9].

are shown.

As mentioned before, this analysis targets a search for supersymmetry with charginos of lifetimes between $10 \text{ cm} \lesssim c\tau \lesssim 40 \text{ cm}$. That means that the charginos decay rather early in the detector, even at the beginning of the tracker. The distinct challenges of such an analysis, shall be listed in the following passage.

First of all, in case R-parity (see Section ??) is conserved, one of the decay products of the chargino, which is the lightest neutralino $\tilde{\chi}_1^0$ is stable, thus travelling through the whole detector only weakly interacting. Therefore it is not detectable. The other chargino decay product, e.g. a pion, can be hardly reconstructed, mainly because it does not origin from the primary vertex (if the chargino reaches the detector before its decay), but secondarily because it is very low in momentum because of the mass-degeneracy between $\tilde{\chi}_1^\pm$ and $\tilde{\chi}_1^0$. The momentum of the decay product is of course highly dependent on the actual mass gap between the neutralino and the chargino. The typical momentum of a pion originating from a chargino to neutralino decay is in the $\tilde{\chi}_1^\pm$ rest frame of the order

$$p_\pi \sim \sqrt{m_{\tilde{\chi}_1^\pm} - m_{\tilde{\chi}_1^0} - m_\pi}.$$

A p_T distribution of the pion for a simulation with $\sqrt{s} = 8$ TeV can be found in Fig. 1.7

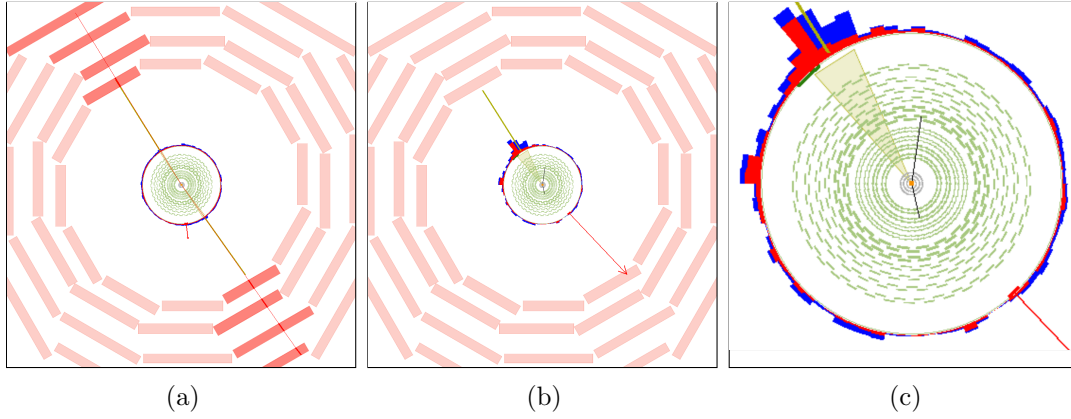


Figure 1.5: Visualisation of possible signatures of a chargino pair produced with a lifetime of $c\tau = 10$ m (a) and a lifetime of $c\tau = 0.5$ m (b and c). In the left picture, both charginos are reconstructed as muons, which can be seen in the energy deposition in the muon chambers (red boxes). In the middle picture both charginos are only visible as tracks in the tracker (black lines), where both trajectories end inside the silicon strip tracker, showing the decay point of the corresponding chargino. The right picture is a zoom of the picture in the middle. Here only the cross-section of the tracker (green wavy lines) is displayed. The red arrow shows the missing transverse energy in the event. The red (blue) towers correspond to the energy deposition in the ECAL (HCAL).

for a mass gap between $\tilde{\chi}_1^\pm$ and $\tilde{\chi}_1^0$ of $\Delta m = 150$ MeV. The p_T distribution peaks at ~ 100 MeV and ends at $p_T \sim 400$ MeV. When the transverse momentum of a particle is very low, the particle trajectory is much more bended compared to a particle with

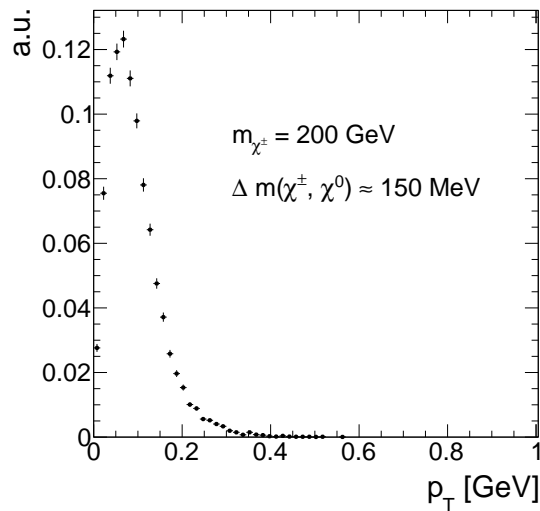


Figure 1.6: Transverse momentum distribution of pions coming from chargino decay into a neutralino with a mass gap of 150 MeV.

higher p_T (see Fig. 1.7 for illustration), thus making the detection of such a particle very challenging. Because of the stronger bending, the track reconstruction efficiency decreases for particles with a transverse momentum below 1 GeV rapidly, ending at around 40% for isolated pions with a p_T of 100 MeV (see [11]).

Taking the hard or even impossible detection of the decay products of the chargino, this lead to the fact, that besides the (short) track of the chargino, nothing can be seen in the detector. Unfortunately, there is no dedicated track trigger at CMS, which makes a specific detection of those events with the help of the chargino track impossible. To be able to search for these models, one therefore needs to take advantage of higher order contributions to the feynman diagrams shown in the previous sections (Figs. 1.2, 1.3), resulting in initial state radiation (ISR). When the initial quarks radiate a high p_T gluon, the resulting jet can be detected and can offer a possibility to search for isolated tracks in the tracker. The non-detection of the chargino's decay products plus a high p_T ISR jet lead additionally to missing transverse energy (MET) in the event. Exploiting these two circumstances, it is possible to detect chargino-pair or chargino-neutralino events with the help of Jet+MET triggers.

To select possible charginos in an event, additional requirements for isolated, high p_T tracks are needed. Those tracks can be eventually disappearing, which means that the track does not cross the full pixel and strip detector. This can happen, when the chargino decays inside the tracker. For very low lifetimes, the tracks can be very short and can have only a few hits in the detector. To define a helical path five parameters are needed, therefore a minimum of three hits are required to be able to reconstruct a particle's trajectory (see [11]).

Furthermore, the massiveness of the charginos shall be exploited in this analysis, on the one hand by selecting only high p_T tracks, but on the other hand by requiring a high energy deposition per path length (dE/dx). The energy deposition depends quadratically on the particle's mass for low velocities ($0.2 < \beta\gamma < 0.9$).

$$\left\langle \frac{dE}{dx} \right\rangle = K \frac{m^2}{p^2} + C$$

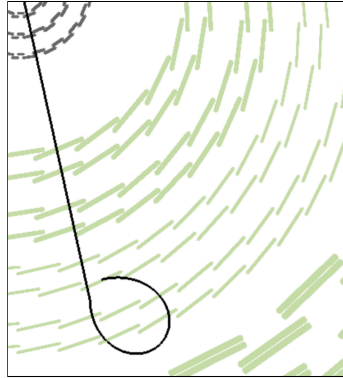


Figure 1.7: Cross-sectional view of the tracker (different tracker layers are illustrated with green lines) and a simulated chargino track (black line) decays to a pion (bended black line).

thus constitute a very nice discriminating variable for massive particles against SM particles.

A specific challenge for this analysis is hence the combination of searching for short tracks and utilising the measurement of the energy deposition of the chargino. For a short track, eventually only passing the first couple layers of the whole tracker system, the pixel tracker becomes obviously very important. This means that a good energy measurement in the pixel system is of great importance to this analysis. However, no other CMS analysis used the energy information of the pixel tracker so far. That means, that a thoroughly study of the quality of the pixel energy calibration needs to be undertaken, and in case the energy calibration is not sufficient, a further energy calibration needs to be carried out.

1.2.1 Comparison to existing searches

As already mentioned before, there are several analyses at CMS at $\sqrt{s} = 8$ TeV with 20 fb^{-1} data, which are sensitive to intermediate lifetime charginos. Most notably, the search for long lived-charged particles [6] and the search for disappearing tracks [7]. An improvement in sensitivity to shorter lifetimes compared to these analysis shall be achieved in a twofold way: First, the selection in this analysis shall also include very short tracks. And secondly, also the inclusion of the variable dE/dx as discriminating variable shall increase the search sensitivity compared to [7].

In [6], for every track a minimum number of eight hits, whereas in [7] a minimum of seven hits were required. This can be very inefficient for shorter lifetimes, where most of the charginos decay already shortly after the pixel tracker. In Fig. 1.8, the normalized distribution of the number of measurements (N_{hits}) is shown. It can be seen, that for lower lifetimes, N_{hits} is peaking at the minimal possible value which is needed for track reconstruction of $N_{\text{hits}} = 3$. For higher lifetimes ($c\tau = 50\text{ cm}$) the distribution shifts to higher values with a second peak at $N_{\text{hits}} \sim 17$. However, a notable fraction of $\sim 40\%$ of tracks has still a number of measurements below $N_{\text{hits}} < 8$.

Additionally, the search for disappearing tracks (which targets models with charginos decaying inside the tracker) did not make use of the high energy deposition of heavy particles. Although this variable was indeed used in the search for long-lived particles, this search was on the other hand not especially designed for intermediate lifetimes (e.g. no muon veto on the selected tracks was required), thus it shows less sensitivity compared to the disappearing track search in the lifetime region between $35\text{ cm} \lesssim c\tau \lesssim 100\text{ cm}$ (see Fig. 1.4).

Therefore to conclude, the general search strategy of the presented analysis is to unite the strategies of [6] and [7] and to lower the strong selection on the number of hits in these analyses to get an optimized selection for lifetimes around $10\text{ cm} \lesssim c\tau \lesssim 40\text{ cm}$.

1.3 Improved dE/dx measurement of short tracks

It was already pointed out, that the inclusion of the pixel energy measurements can increase the sensitivity when searching for short tracks. While the silicon strip detector has already been calibrated as part of the search for long-lived charged particles [6], there was never an offline calibration done for the pixel silicon tracker. To increase the discrimina-

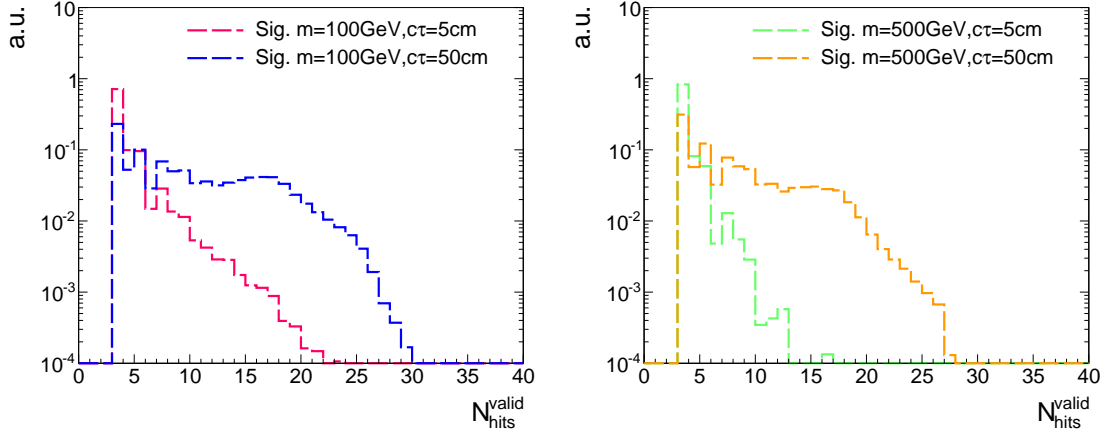


Figure 1.8: Number of measurements in the tracker system N_{hits} for two different signal lifetimes of $c\tau = 5$ cm and $c\tau = 50$ cm and two different masses: 100 GeV (left) and 500 GeV (right). The lower lifetime is much more rapidly falling and peaking at the lowest number of possible measurements of three. For a lifetime of $c\tau = 50$ cm, a second peak at ~ 17 hits appears corresponding to the number of measurements when crossing all pixel barrel (3) and strip inner and outer barrel (6 from stereo and 8 from normal) layers. More information on the generation of the simulated signal samples can be found in Section 1.4.2

tion power of dE/dx , such a calibration procedure was therefore conducted within this PHD thesis.

1.3.1 Measuring dE/dx

The mean energy loss per path length of particles travelling through a layer of material can be described with the Bethe formula [12]:

$$\left\langle \frac{dE}{dx} \right\rangle = kz^2 \frac{Z}{A} \frac{1}{\beta^2} \left[\frac{1}{2} \ln \frac{2m_e c^2 \beta^2 \gamma^2 T_{\text{max}}}{I^2} - \beta^2 - \frac{\delta(\beta\gamma)}{2} \right].$$

It is valid, where the main energy loss originates from ionization effects, i.e. in a region between $0.1 \lesssim \beta\gamma \lesssim 1000$. It is a function of the atomic number (Z) and the atomic mass of the absorber (A). The mean excitation energy (I) for silicon is 173 eV [13]. T_{max} stands for the maximum energy transfer in a single collision. The relevant particle's properties are the velocity (β), the lorentz factor (γ) and the charge (z) of the incident particle. The density correction $\delta(\beta\gamma)$ reduces the mean energy loss at high energies because of polarization effects of the material.

Even if widely used, the mean energy loss is a quantity which is “ill-defined experimentally and is not useful for describing energy loss by single particles” [14]. The problem is caused by the underlying probability distribution of one single dE/dx measurement (this will be named by $\Delta E/\Delta x$ throughout the following sections), which can be parametrized

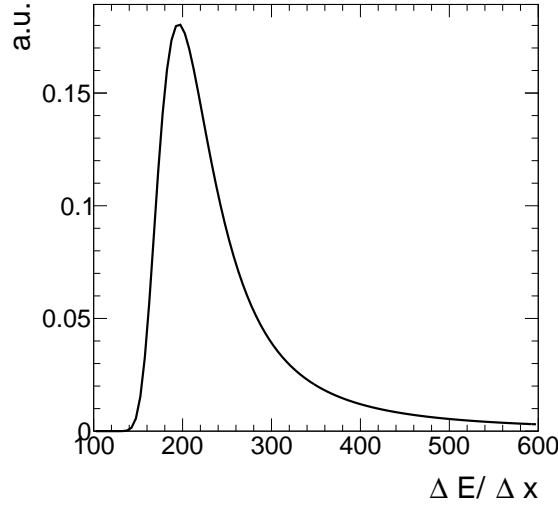


Figure 1.9: Illustration of the shape of a Landau distribution. Parameters were arbitrarily chosen for this figure.

by a Landau distribution [15]

$$p(x) = \frac{1}{\pi} \int_0^\infty e^{-t \log t - xt} \sin(\pi t) dt.$$

The Landau distribution is a highly asymmetric distribution with a long tail towards the right end (see Fig. 1.9). Theoretically it extends to infinite energies, however in nature the maximal deposited energy is of course limited by the particle's full energy. The mean and the variance of a Landau distribution are not defined. Because of its high asymmetry, measurements of $\langle dE/dx \rangle$ with only a few single measurements are easily biased towards high values, making the mean energy loss described by the Bethe formula to a problematic and unstable concept.

A much better observable is the most probable value (MPV): the maximum of the Landau distribution. The MPV is much more stable compared to the mean and is not as easily biased towards higher dE/dx values. The most probable energy loss of a charged particle is defined by the Landau-Vavilov-Bichsel equation [16]:

$$\Delta_p = \xi \left[\ln \frac{2mc^2 \beta^2 \gamma^2}{I} + \ln \frac{\xi}{I} + j - \beta^2 - \delta(\beta\gamma) \right], \quad (1.1)$$

with $\xi = (K/Z)\langle Z/A \rangle(x/\beta^2)$. The thickness of the absorber x appears explicitly in the Landau-Vavilov-Bichsel equation making the most probable energy loss per path length Δ_p/dx logarithmically dependent on x . A comparison between the Bethe mean energy loss $\langle dE/dx \rangle$ and the most probable energy loss Δ_p/dx is shown in Fig. 1.10. However, when measuring tracks with around ~ 15 hits, it is obviously not too simple to extract the most probable value. Large fluctuations can still lead to biases towards higher value of the most probable dE/dx .

There are several "estimators", which try to suppress as much as possible a bias towards

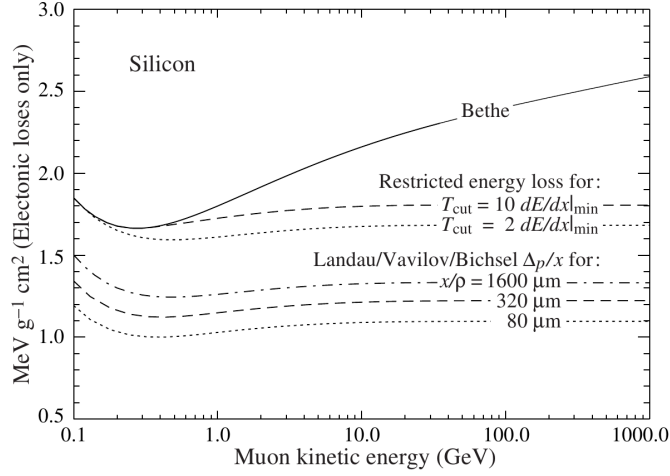


Figure 1.10: Comparison between the Bethe mean energy loss with and without restricted energy loss and the most probable energy loss described by the Landau-Vavilov-Bichsel function for different sizes of thickness. Taken from [14].

the high end, without introducing a bias to lower values. One of the estimator, also used in the next chapter, is the harmonic-2 estimator

$$I_{h2} = \left(\frac{1}{N} \sum_{i=1}^N (\Delta E / \Delta x)_i^2 \right)^{-1/2}, \quad (1.2)$$

where $\Delta E / \Delta x$ correspond to one measurement in one tracker module. The harmonic mean of all N measurements with the power of 2 is then the estimated most probable dE/dx .

SM particles as pions and muons are minimal ionising in silicon for $\beta\gamma \sim 4$ (see Fig. 1.11). For higher momenta the deposited energies increase again reaching a plateau at around $\beta\gamma \sim 100$. However, new heavy charged particles would mainly be unrelativistic because of their high mass and would therefore deposit much higher energies in the detector. This makes dE/dx a very well discriminating variable. Thus, the energy loss per path length can be used to discriminate between SM particles and new heavy charged particles, which are usually unrelativistic because of their high mass.

1.3.2 Gain calibration of the silicon pixel tracker

During Run I in 2012, the pixel silicon detector was continuously subjected to an energy calibration, a so-called gain calibration. Every pixel was calibrated to the same response, such that the whole pixel tracker should have been well inter-calibrated. Unfortunately, due to various reasons, such as the imperfect constancy of the reference signal, or radiation and temperature induced changes, the energy calibration could not ensure a fully calibrated pixel tracker. This imperfection of the gain calibration can be seen in Fig. 1.12, where the sum of the harmonic-2 estimator for all tracks $\sum_{\text{all trks}} I_{h2}$ over the full data-taking period in 2012 is shown. Four different steps can be spotted. The first and the third steps correspond

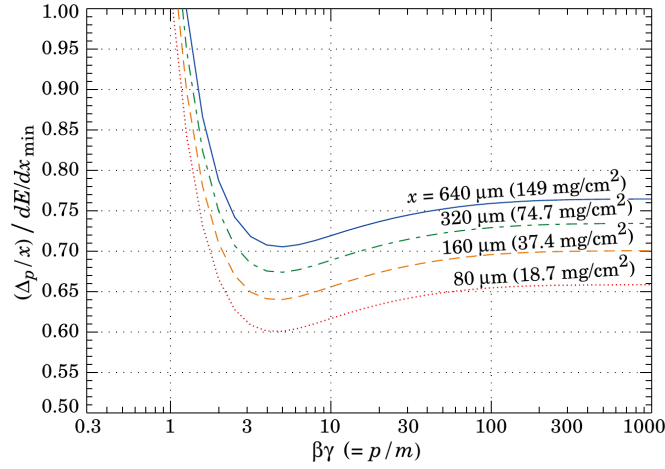


Figure 1.11: Most probable energy loss in silicon, scaled to the mean loss of a minimal ionizing particle ($388 \text{ eV}/\mu\text{m}$). Taken from [14].

to changes in the settings of the tracker due to irradiation. The second and fourth step show the moment where an online gain calibration was again applied. Unfortunately, although a gain calibration was carried out (even with some delay), it could not bring the average dE/dx to the same level before the changes in the settings occurred. The size of the difference in the dE/dx measurement over time being around 15% is too large to use dE/dx without a further calibration.

In the following sections the method of the gain calibration (splitted into an section about the inter-calibration of gain and the absolute calibration of gain) of the pixel silicon tracker is explained. Detailed technical information about the pixel tracker can be found in Section ??.

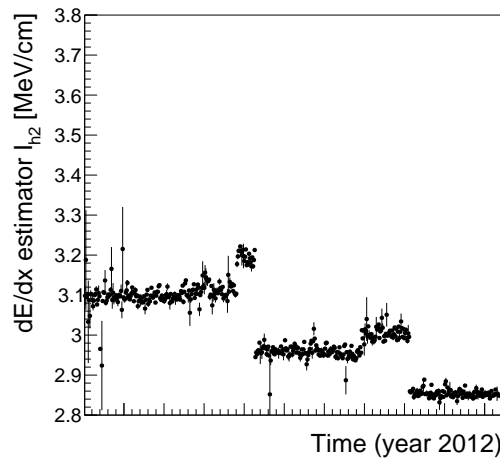


Figure 1.12: Sum of all track's dE/dx (harmonic-2 estimator) over the full year 2012. Only pixel hits are taken into account. Every data point corresponds to one run.

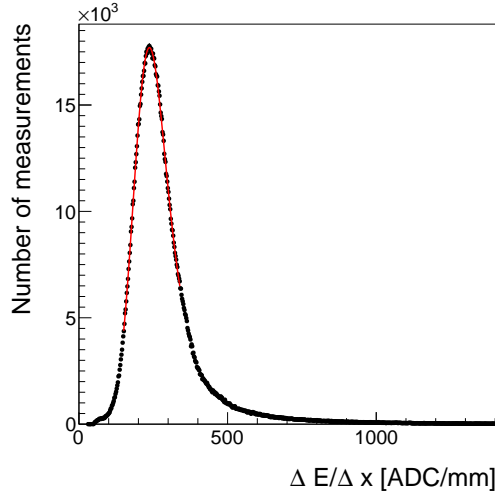


Figure 1.13: An example of the $\Delta E/\Delta x$ distribution measured in ADC count per mm for one module of the CMS pixel tracker. A Landau convoluted with a Gaussian is fitted to the core of the distribution in an iterative procedure.

Inter-calibration of gain

The main goal of the gain calibration is to get a uniform response in the ionization energy loss dE/dx over the full data taking period in 2012. To ensure also a uniform response of all modules within one time step, also an inter-calibration on module level was carried out. The inter-calibration can in principle be done on various stages: the highest granularity would be a calibration on pixel level, followed by a calibration on ROC-level and then on module-level. Lower granularities in descending order are rings (modules with same z-position) and finally layers (3 layers in the barrel and 4 disks in the endcap). It was checked that all pixels and all ROCs (on one module) are well inter-calibrated, such that the inter-calibration was finally done module-wise. The applied method for the gain calibration of the pixel tracker follows closely the method in [17].

The gain calibration of the pixel silicon tracker has been carried out with the help of minimal ionising particles (MIPs). MIPs in this context are not defined as particles depositing a minimum amount of energy, but more generally a small amount of energy. This denotes all particles located at the plateau of the dE/dx distribution vs. momentum (see Fig. 1.11). It ensures that all particles deposit a rather similar amount of energy such that the variation due to different momenta is suppressed. The small ionisation for particles was ensured with a momentum selection of $p > 2$ GeV. Additionally, only tracks with at least eight hits and a $\chi^2/n.d.o.f. < 3$ to ensure a good reconstruction were used. For the calibration a sample containing around 50 million “minimum bias” events is used which is specifically recorded for tracker calibration purposes. “Minimum bias” means that neither an online nor offline selection was applied.

For every module in the pixel tracker (there are 1440 modules in total), a distribution of the energy loss per path length $\Delta E/\Delta x$ is built. Figure 1.13 shows an example distribution for one module. The underlying Landau distribution can be nicely seen. To extract the MPV for every module a fit to the core distribution is performed. The fit is done with a

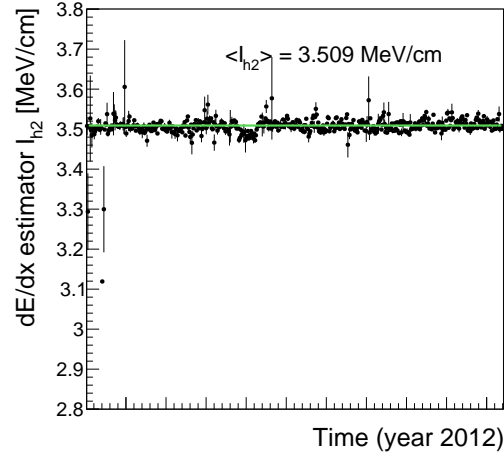


Figure 1.14: Sum of all track's dE/dx (harmonic-2 estimator) over the full year 2012 after applying the calibration factors, resulting in an average dE/dx of 3.51 MeV/cm. Only pixel hits are taken into account. Every data point corresponds to one run.

Landau convoluted with a Gaussian function to be closer to the experimentally observed energy spectrum. This also increases the fit performance and the stability of the fit. The measurement of $\Delta E/\Delta x$ is done in ADC counts per mm. ADC counts are a measure for the deposited charge after digitization. It consists out of a unsigned 16-bit integer (ranging from 0 to 65 535). The path length Δx is calculated with

$$\Delta x = d_{\text{module}_i} \cdot \cos(\phi_{\text{track}}),$$

where d_{module_i} is the thickness of module i and ϕ_{track} is the relative angle of the particle's trajectory to the axis normal of the module. With the measured MPV extracted from the fit, an inter-calibration factor is calculated for every module

$$c_{\text{inter}} = \frac{\text{MPV [ADC/mm]}}{\text{MPV}_{\text{target [ADC/mm]}}} = \frac{\text{MPV [ADC/mm]}}{300 \cdot 265 \text{ ADC/mm}}.$$

The factor $300 \cdot 265 \text{ ADC/mm}$ is in principal an arbitrary number. However, it was chosen such that it corresponds approximately to the most probably energy deposition of a MIP. The calibration factor can then be used to scale every single measurement in a module to a calibrated $\Delta E/\Delta x$ measurement

$$\frac{\Delta E}{\Delta x_{\text{calibrated}}} = \frac{\frac{\Delta E}{\Delta x_{\text{uncalibrated}}}}{c_{\text{inter}}}$$

The determination of the calibration factor needs to be done for every of the five time steps, shown in Fig. 1.12 independently, in order to get rid of the time dependency. The result of the inter-calibration can be seen in Fig. 1.14. The variation over time was indeed eradicated, resulting in a maximal time variation of less than $\sim 1\%$.

Additionally, the same procedure is carried out for a corresponding simulated data sample to ensure also the inter-calibration of the pixel modules on all simulated samples.

Absolute calibration of gain

As a final step, the targeted MPV being $\text{MPV}_{\text{target}} = 300 \cdot 265 \text{ ADC/mm}$ needs to be translated to a meaningful physical quantity given in physical units (e.g. MeV/cm). That means, that the charge measurement in ADC counts needs to be converted to the real energy release of a particle. The relation between ΔE in ADC counts and the energy loss in eV is given by

$$\Delta E [\text{eV}] = \frac{\Delta E [\text{ADC}]}{c_{\text{inter}}} \cdot \frac{N_e}{\text{ADC}} \cdot 3.61 \text{ eV},$$

where N_e/ADC is the number of electrons which correspond to one ADC count and 3.61 eV is the mean energy needed to create one electron-hole pair in silicon at -10°C . Such an absolute gain calibration can be done with the help of several methods (all explained in [17]). For the absolute calibration of the silicon pixel tracker, it can be taken advantage of the already conducted absolute calibration of the silicon strip detector. In [17], the absolute gain calibration was done with the help of the most probable energy release per path length of muons, theoretically described by the Landau-Vavilov-Bichsel formula in Eq. 1.1. To calibrate the pixel tracker to the correct energy loss per path length it is therefore sufficient to determine one calibration factor to relate the average dE/dx of all tracks in the pixel tracker as shown in Fig. 1.14 to the average measured dE/dx in the strip tracker, shown in Fig. 1.15 by

$$c_{\text{absolute}} = \frac{dE/dx_{\text{strip}}}{dE/dx_{\text{pixel}}} = \frac{3.303}{3.509} = 0.941.$$

This factor is then applied on top of c_{inter} for all pixel modules.

Finally, also for the simulated samples an absolute calibration factor needs to be determined, where the simulated pixel tracker is calibrated to the average dE/dx of the silicon strip measured in data.

1.3.3 Asymmetric Smirnov discriminator

As mentioned before, a difficult task when measuring the energy deposition of a particle consists in finding a robust estimator for the MPV of the underlying Landau, i.e. combining eventually only a few single measurements of $\Delta E/\Delta x$ to one single dE/dx estimator. The harmonic-2 estimator I_{h2} was already introduced in Section 1.3.1 in Eq. 1.2. It is known as a robust estimator not easily biased by large fluctuation in $\Delta E/\Delta x$ because of the suppression by a factor of 2.

However, it was shown in [17] that a better discrimination between SM particles and possible new heavy particles can be achieved when using likelihood techniques, i.e. determining the probability that the set of all $\Delta E/\Delta x$ belonging to one track is actually compatible with the hypothetical probability distribution of a MIP.

Testing that a measured sample has been drawn from a specific distribution is known as the Smirnov-Cramér-von Mises test [18,19], which is deduced from the integral of the

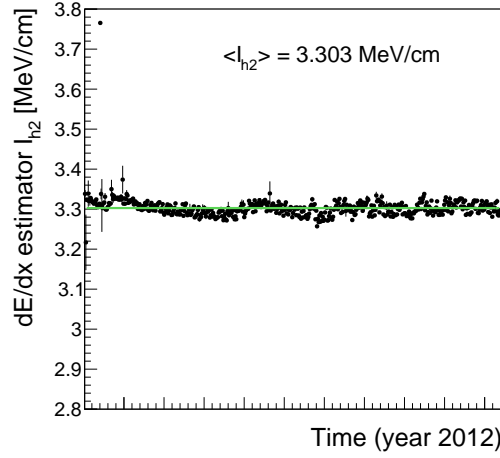


Figure 1.15: Sum of all track's dE/dx (harmonic-2 estimator) measured in the silicon strip detector over the full year 2012. The average most probable dE/dx is $I_{h2} = 3.303 \text{ MeV/cm}$. Every data point corresponds to one run.

squared difference of the measured distribution $P_N(x)$ to the hypothesis distribution $P(x)$

$$I_s = \int_{-\infty}^{\infty} [P_N(x) - P(x)]^2 dP(x)$$

leading to a test statistics of

$$I_s = \frac{3}{N} \cdot \left(\frac{1}{12N} + \sum_{i=1}^N \left[P_i - \frac{2i-1}{2N} \right]^2 \right),$$

where P_i is the cumulative probability that a MIP would release a $\Delta E/\Delta x$ equal or smaller than the measured $\Delta E/\Delta x$ with all P_i are arranged in increasing order.

However, this test statistics is not sensitive to whether there are incompatibilities because of higher or lower variations compared to the hypothesis distribution. It is therefore not really suitable for the discrimination between MIPs and heavy new particles by dE/dx . A so-called Asymmetric Smirnov-Cramér-von Mises discriminator was developed in [17] which is only sensitive to incompatibilities to the MIP hypothesis towards higher energy depositions

$$I_{as} = \frac{3}{N} \cdot \left(\frac{1}{12N} + \sum_{i=1}^N \left[P_i \cdot \left(P_i - \frac{2i-1}{2N} \right)^2 \right] \right).$$

A value of I_{as} close to zero indicates good compatibility with the MIP hypothesis, whereas a value close to one indicates worse compatibility because of too large energy loss.

The underlying probability distribution of the energy release for a given path length in the pixel tracker is extracted from the same “Minimum bias” sample used for the pixel energy calibration. In total 28 different templates each for a different given path length

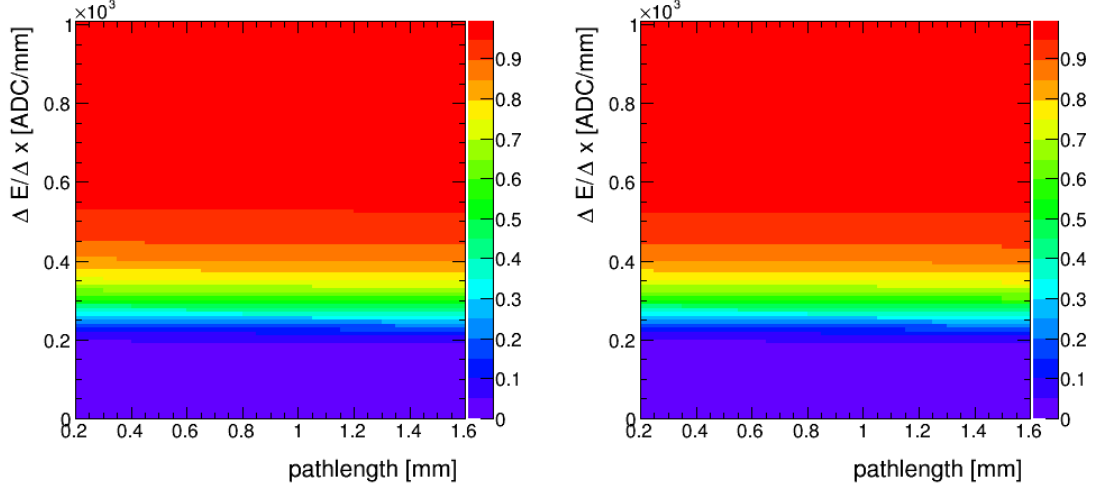


Figure 1.16: Cumulative probability for a MIP to release a $\Delta E/\Delta x$ (y-axis) vs. the pathlength (x-axis) in data (left) and simulation (right) for the pixel tracker.

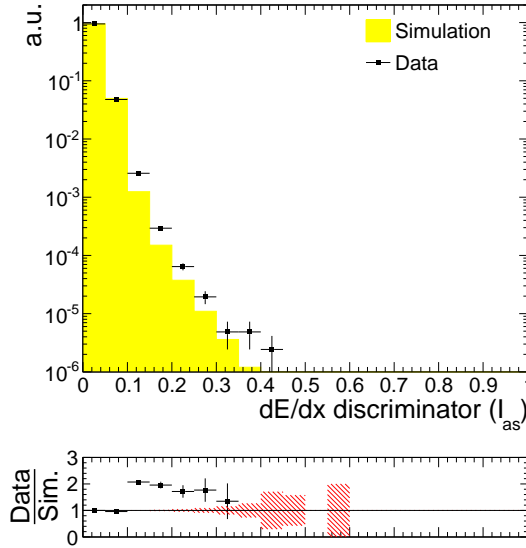


Figure 1.17: Normalized I_{as} distribution for MIPs from the minimum bias sample in data and simulation for good quality tracks with $p > 5$ GeV and $|\eta| < 2.1$.

are created. The corresponding templates for the energy release in the silicon strip detector were already built by [17]. In Fig. 1.16 the probability distribution template for the pixel tracker in data and simulation is shown. A comparison between the energy release by MIPs (I_{as}) in data and simulation for good quality tracks (high-purity as defined in [20] and minimum number of eight hits) with $p > 5$ GeV and $|\eta| < 2.1$ can be found in Fig. 1.17. dE/dx shows good agreement in data and simulation for $I_{\text{as}} < 0.1$. For larger values, I_{as} shows a larger decrease in simulation than in measured data. That's the reason

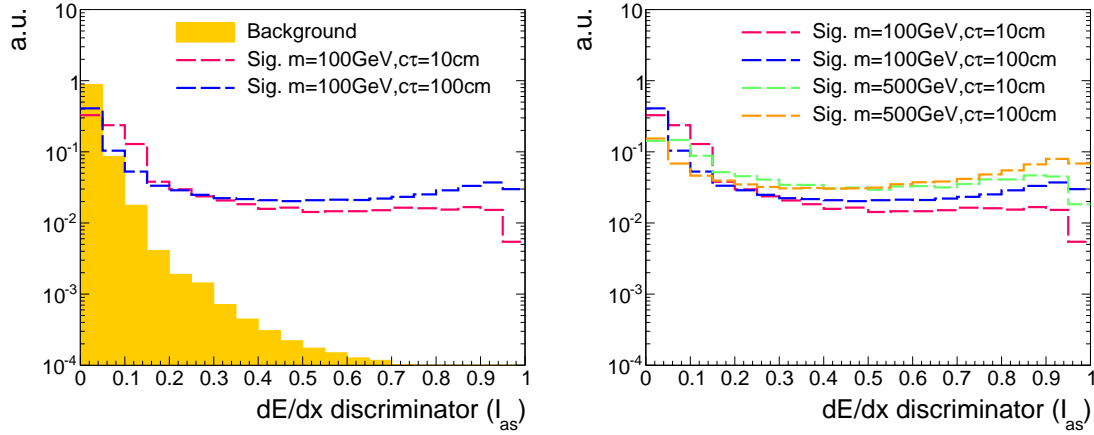


Figure 1.18: Normalized I_{as} distribution for simulated background and signal tracks (left) and for four different signal models (right) for high-purity tracks (as defined in [20]) with $p_T > 10$ GeV and $|\eta| < 2.1$. For the illustration of the background tracks' spectrum simulated $t\bar{t}$ +jets events are used (more information about this sample is given in Section ??).

why a data-based approach for analyses exploiting dE/dx information is needed.

1.3.4 Efficiency improvements

The goal of including the pixel energy information is to increase the discrimination power of I_{as} between background and signal tracks, especially for shorter lifetimes. In Fig. 1.18, a comparison of the shapes of the energy release by MIPs and by signal tracks in simulation is shown (details about the simulated samples can be found in the next section Section 1.4.2). It can be seen, that the I_{as} distributions of the all signal models show a much longer tail toward $I_{as} = 1$, whereas the background is rapidly falling. Not only the mass of the signal track influences the I_{as} distribution but also the number of hits and the velocity (β) distribution of a signal model. The influence of the velocity can be easily seen in Eq. 1.1. This in turn results in the dependency of I_{as} on the mass of the chargino. But also for models with the same mass, the velocity is higher in average for shorter lifetimes. This is caused by the fact, that for shorter lifetimes (e.g. $c\tau = 10$ cm), already a sizeable fraction of the charginos decay before reaching the tracker system. The probability of reaching the detector increases for higher velocities, which can be clearly seen at the survival probability

$$P(t) = e^{-\frac{t}{\gamma\tau}}, \quad (1.3)$$

which shows that the survival probability is increasing for increasing β . That means shorter lifetimes lead to higher average β which in turn lead to lower I_{as} .

The number of measurements in the tracker system defines the influence of single fluctuations in $\Delta E/\Delta x$ on the I_{as} discriminator. Because of the large right tail of the Landau distribution, for tracks with a low number of hits this leads to higher I_{as} due to the fluctuations in the energy release.

That means that for models with lower lifetimes of the chargino there are two different effects: first, due to the smaller number of measurements the chargino tends to higher I_{as} values, second for low lifetime, the velocity distribution of those charginos reaching the detector is in average higher, which in turn leads to lower I_{as} values. Both effects can be seen in Fig. 1.18 (right). The large tail for longer lifetimes is caused by the lower velocities, but the small surplus between 0.1 and 0.2 is caused by the smaller number of measurements for lower lifetimes.

Finally, the impact of the additional $\Delta E/\Delta x$ information from the pixel tracker on the selection efficiency of signal and background tracks shall be quantified. Figure 1.19 shows the signal selection efficiency against the background selection efficiency for different selection cuts in I_{as} , once including the pixel information and once without it. A previous selection of good quality tracks and $p_{\text{T}} > 10 \text{ GeV}$ is applied. The background selection efficiency is estimated with simulated W +jets events but was additionally checked on simulated $t\bar{t}$ +jets and QCD-multijet events (further information about the simulated samples can be found in the next section). No significant difference between these processes in the background selection efficiency was observed.

The signal selection efficiency and the background suppression depend on the mass and the lifetime of the charginos. The discrimination power of I_{as} is as expected much better for higher masses. In addition, the impact of the inclusion of the pixel energy information is already for looser selections in I_{as} visible in the higher mass case. However, the additional energy information shows similar impact for very strong selections for all lifetimes and masses.

For high chargino masses and small signal selection efficiencies, the background suppression can be improved up to a factor of 20. For looser selections leading to higher signal efficiency of 40%, the gain in the suppression reduces to a factor of 10.

1.4 Simulated samples

For the investigation of the various backgrounds, the analysis relies also on simulated samples. An extensive introduction to the techniques and tools required for the simulation of SM and beyond SM processes can be found in Section ??.

In the following two sections an overview about the SM (Section 1.4.1) and SUSY samples (Section 1.4.2) used to design the search is given. All samples are reweighted to match the measured distribution of primary vertices in data.

1.4.1 SM Background samples

To investigate the sources of background, various simulated SM samples are used. In order to have the possibility to make use of the dE/dx variables, a special data format of the simulated samples is required (called RECO format). Unfortunately, not all SM processes were available in this format in which also the information about the energy release in the tracking system is included. However, as this analysis needs to rely anyways on a data-based background estimation method, because of the limited quality of the dE/dx simulation, it does not constitute a serious problem, but only limit the possibility of an

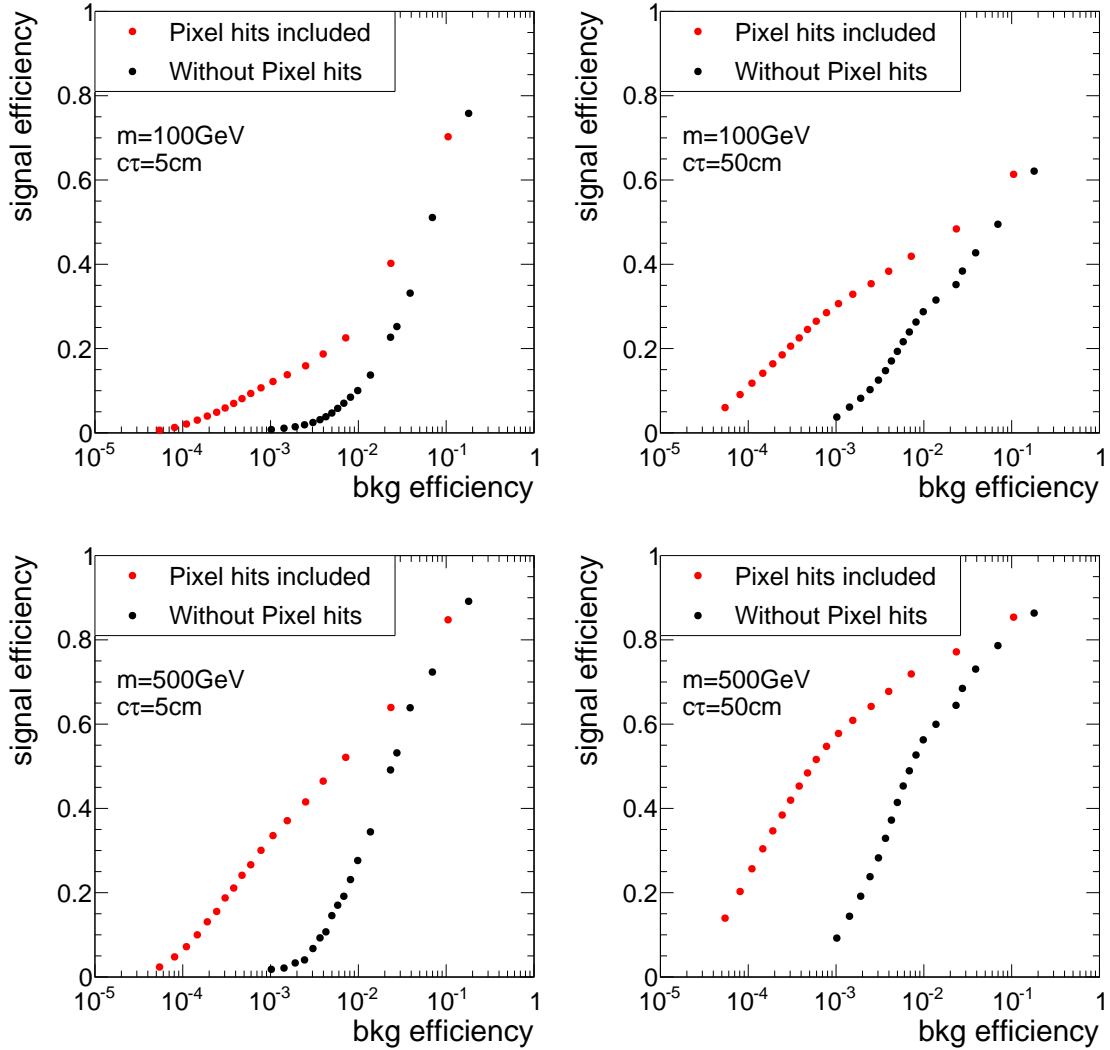


Figure 1.19: Signal selection efficiency vs. background selection efficiency when scanning through different selections in I_{as} for four different signal models.

extensive comparison between data and simulation going beyond shape comparisons.²

In Table 1.1 all SM samples are listed which were available in the RECO format and are used in the analysis. Due to the immense size of the samples (between 5 and 70 TB) and in order to match a reasonable storage space a reduction was done by selecting only events which contain at least one leading jet with a minimum transverse momentum of $p_T > 60$ GeV.

In addition, further simulated samples not containing the energy information are used. These are needed to study the background inclusively in the variable I_{as} . They are listed in Table 1.2.

²E.g. the background process $Z \rightarrow \nu\nu$ sample is not available, which can possibly contribute via the fake background to the search. However, as the rate of fakes is independent of the underlying process, this background can be studied with the same quality with a $W + \text{jets}$ sample.

1.4.2 Signal samples

For the investigation of a possible signal, events containing either chargino pair production $q\bar{q} \rightarrow \tilde{\chi}_1^\pm \tilde{\chi}_1^\mp$ or chargino neutralino production $q\bar{q} \rightarrow \tilde{\chi}_1^\pm \tilde{\chi}_1^0$ are simulated. The simulation is done with the matrix-element event generator MADGRAPH [23]. The parton showering and hadronization processes are then simulated with Pythia 6 [24]. A last step is needed to simulate the interactions of the generated particles with the detector material, which is done with GEANT4 [25, 26].

Furthermore, a special treatment for long-lived particles is required. In order to get the right detector simulation of the energy loss of the long-lived particles which decay after the beam pipe, the lifetime of the chargino cannot be set in the matrix-element generator but needs to be specified within GEANT4. This also means, that the decay products are only existing in the detector simulation, but are not accessible as particles in the event generators.

To narrow down the required computing sources, the simulation was only done for a few lifetimes (1 cm, 5 cm, 10 cm, 50 cm, 100 cm, 1 000 cm and 10 000 cm). To get still a tight scan over the lifetime space, other lifetimes were generated using lifetime reweighting. This can be done by determining for every event a weight which is depending on the individual proper lifetime of the chargino (in case of chargino pair production it depends on the individual lifetime of the two charginos). The event weight is given by

$$w = \prod_{i=1}^n \frac{\tau^{\text{gen}}}{\tau^{\text{target}}} \cdot \exp \left[t_i \cdot \left(\frac{1}{\tau^{\text{target}}} - \frac{1}{\tau^{\text{gen}}} \right) \right],$$

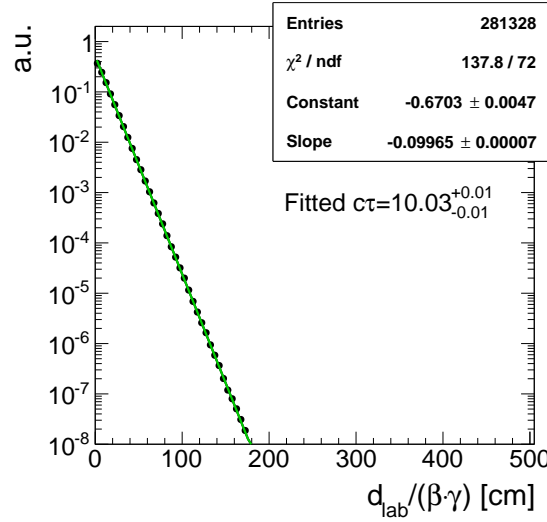
where n is the number of charginos in the event, τ^{gen} is the generated mean lifetime in the particle's rest frame and t_i is the individual proper lifetime of the chargino. The resulting mean lifetime is then given by τ^{target} . A derivation of this formula can be found in Appendix ???. With the reweighting procedure a tight covering of the lifetime space could be achieved with lifetimes of $c\tau = a \cdot 10^n$ for $n=0,1,2,3,4$ and $a=[1,9]$. Figure 1.20 shows the exponential distribution of the individual proper lifetime of the charginos after reweighting a simulated sample with $c\tau^{\text{gen}} = 50$ cm to a lifetime of $c\tau^{\text{target}} = 10$ cm. Fitting the exponential spectrum should result in the correct mean proper lifetime as parameter of the fit. It can be seen, that the reweighting procedure can reproduce the targeted lifetime

Table 1.1: Available Standard Model background samples containing $\Delta E/\Delta x$ information which are used for background estimation studies.

Process	Cross section [pb]	$\mathcal{O}_{\text{calculation}}$
$W + \text{jets}$	36703.2	NNLO [21]
$t\bar{t} + \text{jets}$	245.8	NNLO [22]
$Z \rightarrow \ell\ell$ ($\ell = e, \mu, \tau$)	3531.9	NNLO [21]
QCD ($50 \text{ GeV} < \hat{p}_T < 1400 \text{ GeV}$)	9374794.2	LO

Table 1.2: Standard Model background samples without $\Delta E/\Delta x$ information.

Process	Cross section [pb]	$\mathcal{O}_{\text{calculation}}$
$W + \text{jets}$	36703.2	NNLO [21]
$Z \rightarrow \ell\ell$ ($\ell = e, \mu, \tau$) + 1,2,3,4 jets	3531.9	NNLO [21]

Figure 1.20: Normalized distribution of the proper lifetime $d_{\text{lab}}/(\beta\gamma)$ of all charginos contained in a signal sample with a generated lifetime of $c\tau^{\text{gen}} = 50$ cm reweighted to a lifetime of $c\tau^{\text{target}} = 10$ cm.

of 10 cm.

All samples were generated for different chargino masses always almost mass-degenerate to the lightest neutralino. The mass gap between chargino and neutralino was set to 5 GeV. However, as this analysis does not make use of the other decay products and the lifetime is set in GEANT4, the mass gap does not play any role. Six different masses from 100 GeV to 600 GeV are simulated. This leads then to a total number of 42 signal samples. In Table 1.3 the NLO-NLL³ cross sections at $\sqrt{s} = 8$ TeV for $\tilde{\chi}_1^\pm \tilde{\chi}_1^\mp$ and $\tilde{\chi}_1^\pm \tilde{\chi}_1^0$ production with wino-like charginos and degeneracy between $m_{\tilde{\chi}_1^\pm}$ and $m_{\tilde{\chi}_1^0}$ are listed [27, 28]. The cross section does not depend on the lifetime of the chargino.

³NLO: next-to-leading order, NLL: next-to-leading logarithmic accuracy

Table 1.3: Produced signal simulated samples with corresponding cross sections

$m_{\tilde{\chi}_1^\pm}$ [GeV]	$\sigma_{\tilde{\chi}_1^\pm \tilde{\chi}_1^\mp}$ [pb]	$\sigma_{\tilde{\chi}_1^0 \tilde{\chi}_1^\mp}$ [pb]
100	5.8234	11.5132
200	0.37924	0.77661
300	0.06751	0.14176
400	0.01751	0.03758
500	0.00553	0.01205
600	0.00196	0.00431

1.5 Event selection

1.5.1 Datasets and triggers

The analysis is performed on pp collision data recorded in the year 2012 at the CMS experiment for a center-of mass energy of $\sqrt{s} = 8$ TeV. In total an integrated luminosity of 19.7 fb^{-1} was recorded in 2012.

As outlined in Section 1.2, already on trigger level, the detection of chargino tracks is a challenging task. The direct detection of events containing chargino tracks on trigger level is not possible because there were no information at CMS about the tracking system on L1 level available. Furthermore, there is no intrinsic missing transverse energy in the event, when the chargino (or both charginos) decay inside the trigger. Therefore, the detection of these events shall be achieved with the help of the radiation of the initial state quarks. When initial state radiation occurs, it is possible to trigger on a high- p_T jet and also on \cancel{E}_T in the event.

For this purpose, several triggers are exploited. It is required that at least of them must have fired to consider the event in the analysis. In Table 1.4, the triggers are listed together with the recorded corresponding integrated luminosity in the time when they were active.

Table 1.4: \cancel{E}_T and \cancel{E}_T +jet triggers used in the analysis together with the recorded corresponding integrated luminosity in the time when they were in place.

Trigger	Luminosity [fb^{-1}]
HLTMonoCentralPFJet80_PFMETnoMu95_NHEF0p95	5.3
HLTMonoCentralPFJet80_PFMETnoMu105_NHEF0p95	14.4
HLT_MET120_HBHENoiseCleaned	19.7

The HLTMonoCentralPFJet80_PFMETnoMu95_NHEF0p95 and HLTMonoCentralPFJet80_PFMETnoMu105_NHEF0p95 triggers exploit both the L1 ETM40 trigger, which requires the missing energy to be larger than 40 GeV. On HLT level, they require further a least on PF jet with $p_T > 80$ GeV and the PF missing transverse momentum \cancel{E}_T (not taken into account the p_T of any muon in the event) to be larger than 95 GeV (or 105 GeV). Finally, the energy release by neutral hadrons must not be larger than 95% for all jets in the event. The HLTMonoCentralPFJet80_PFMETnoMu95_NHEF0p95 trigger was in place during Run A and Run B in 2012 data taking, whereas HLTMonoCentralPFJet80_PFMETnoMu105_NHEF0p95 was set during Run C and Run D in 2012.

The HLT_MET120_HBHENoiseCleaned trigger is based on the two L1 triggers ETM40 and ETM36 which are combined by a logical OR. On HLT level, the trigger requires that the missing energy measured in the calorimeter is larger than 120 GeV. The HBHENoise filter reduces background from electronic noise in the HCAL.

Table 1.5 lists the datasets in which the triggers used in the analysis are comprised. Again, because of the size of the datasets (150.5 TB in total), a reduction of the size is

Table 1.5: MET data samples used in the search with the contained integrated luminosity.

Dataset	Luminosity [fb^{-1}]
/MET/Run2012A-22Jan2013-v1/RECO	0.876
/MET/Run2012B-22Jan2013-v1/RECO	4.412
/MET/Run2012C-22Jan2013-v1/RECO	7.055
/METParked/Run2012D-22Jan2013-v1/RECO	7.354

achieved by selecting only events with at least one jet with a minimum p_T of 50 GeV.

In addition, the analysis makes use of the datasets listed in Table 1.6. These datasets are used for background estimation purposes and the estimation of their associated systematic uncertainties.

1.5.2 Analysis selection

In order to suppress events originating from SM processes (such as QCD-multijet events, $W + \text{jets}$, etc.), a selection for signal-like tracks is applied which shall be described in the following sections. The candidate track selection follows closely the selection required in [7].

Event based selection

First, to suppress cosmic events and noise from the beam halo a selection on the quality of the vertex can be applied. This selection includes requirements of the position of the

Table 1.6: Further datasets used for background estimation.

Dataset	Luminosity [fb^{-1}]
/SingleMu/Run2012A-22Jan2013-v1/AOD	0.876
/SingleMu/Run2012B-22Jan2013-v1/AOD	4.405
/SingleMu/Run2012C-22Jan2013-v1/AOD	7.040
/SingleMu/Run2012D-22Jan2013-v1/AOD	7.369
/SingleElectron/Run2012A-22Jan2013-v1/AOD	0.876
/SingleElectron/Run2012B-22Jan2013-v1/AOD	4.412
/SingleElectron/Run2012C-22Jan2013-v1/AOD	7.050
/SingleElectron/Run2012D-22Jan2013-v1/AOD	7.368

vertex with respect to the beam axes and the number of degrees of freedom (which is strongly correlated to the number of tracks originating from the vertex) [29]:

- ❖ The vertex must have at least four degrees of freedom: vtx with ≥ 4 d.o.f.
- ❖ The position of the vertex along the beam line must be within 24 cm from the beam origin: $|dz| \leq 24$ cm.
- ❖ The position in the transverse direction must be within 2 cm from the beam origin: $|d0| \leq 2$ cm.

After these selection cuts are applied the remaining events are subjected to a further pre-selection.

To maximise the signal acceptance, the trigger related selection cuts are chosen as close as possible to the trigger thresholds (see Sec. 1.5.1). In Fig. 1.21, the distributions of \cancel{E}_T and the transverse momentum of the leading jet $p_T^{1,\text{jet}}$ are shown for different signal models. Only jets are taken into account with $|\eta| < 2.4$ and which fulfill several further criteria:

- Charged hadron energy fraction > 0.2
- Charged electromagnetic energy fraction < 0.5
- Neutral hadron energy fraction < 0.7
- Neutral electromagnetic energy fraction < 0.7 .

These requirements ensure that noise from cosmics and beam halo is suppressed [30]. In can be seen in Fig. 1.21 that already for a selection of $\cancel{E}_T > 100$ GeV 80% of the signal events are rejected.

The trigger efficiency as a function of PF MET and $p_T^{1,\text{jet}}$ was determined within [31] with a single-muon reference sample. The trigger paths become fully efficient for $p_T^{1,\text{jet}} \gtrsim 110$ GeV and $\cancel{E}_T \gtrsim 220$ GeV [30].

However, as said before, this search imposes a trigger selection to maximise the signal acceptance:

- ❖ In every event needs to be at least one jet within $|\eta| < 2.4$ with transverse momentum larger than 110 GeV which fullfils the above mentioned noise cleaning criteria: $p_T^{1,\text{jet}} > 110$ GeV
- ❖ The missing transverse momentum must be larger than 100 GeV: $\cancel{E}_T > 100$ GeV

Because of the huge cross-section, Multijet events are frequently produced at the LHC. Due to jet energy mismeasurements, they can also contribute to data samples recorded with MET triggers. Therefore, some special requirements to suppress events emerging from strong production processes are enforced. QCD-multijet events can be characterized by topologies where two jets are almost back-to-back. Additionally, in QCD-multijets events the missing energy is usually aligned with one of the leading jets in the event. Therefore the following two requirements are sufficient to suppress QCD-multijet events efficiently.

- ❖ $\Delta\phi$ between any of two subleading jets (with $p_T < 20$ GeV and $|\eta| < 4.5$) in the event must be smaller than 2.5: $\Delta\phi(j_i, j_j) < 2.7$.
- ❖ $\Delta\phi$ between any of the two leading jets (with $p_T < 20$ GeV and $|\eta| < 4.5$) and the \cancel{E}_T must be larger than 0.5: $\Delta\phi(j_{1,2}, \vec{\cancel{E}}_T) > 0.5$.

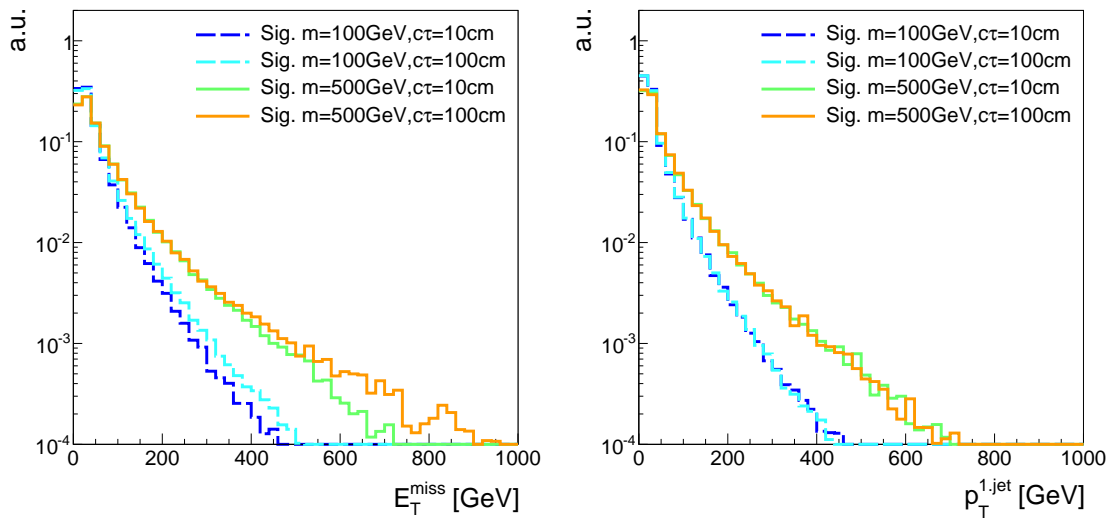


Figure 1.21: Distribution of missing transverse momentum (left) and the transverse momentum of the leading jet (right) for four different signal samples

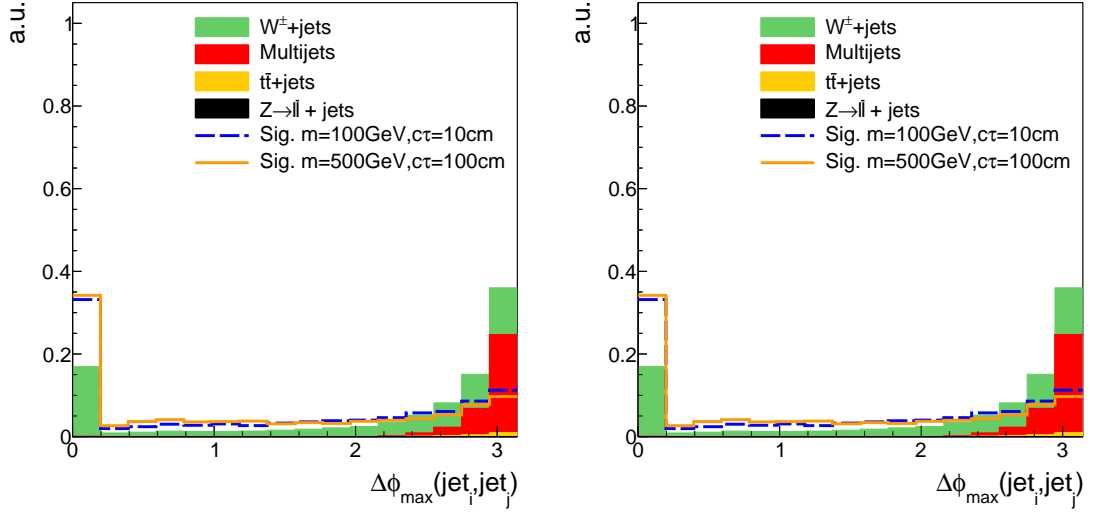


Figure 1.22: Maximal $\Delta\phi$ between any of two subleading jets (left) and the minimal $\Delta\phi$ between the \cancel{E}_T vector and the first two jets (right) normalized to unit area after the trigger selection.

In Fig. 1.22, the maximal $\Delta\phi$ of any of two subleading jets and the minimal $\Delta\phi$ between the \cancel{E}_T vector and the first two subleading jets for the QCD-multijet data set and two different signal datasets is shown.

Selection of high quality and non SM-like tracks

After the reduction of background processes with event based variables, a track based selection is carried out. To get an optimized selection for possible chargino tracks several signal track characteristics are exploited.

First a selection of tracks of good quality is enforced:

- ❖ The track must be of “high purity” as defined in [20].
- ❖ The track is required to have no missing middle or inner hits: $N_{\text{miss}}^{\text{middle/inner}} = 0$
- ❖ The radial and longitudinal distance of the track to the primary vertex must be small: $|d0| < 0.02 \text{ cm}$, $|dz| < 0.5 \text{ cm}$.
- ❖ Only tracks are considered which are within the tracker acceptance taken also an isolation cone into account: $|\eta| < 2.1$.
- ❖ A first loose selection of tracks in the transverse momentum is applied: $p_T > 10 \text{ GeV}$.

In Figs 1.23, 1.24 and 1.25, the power of the various track selection cuts are shown.

Finally, to reject background tracks emerging from SM processes, an electron, muon and tau veto is applied. That means all candidate tracks are rejected when they are in a cone of $\Delta R < 0.15$ around a reconstructed electron, muon or tau. Additionally, the candidate

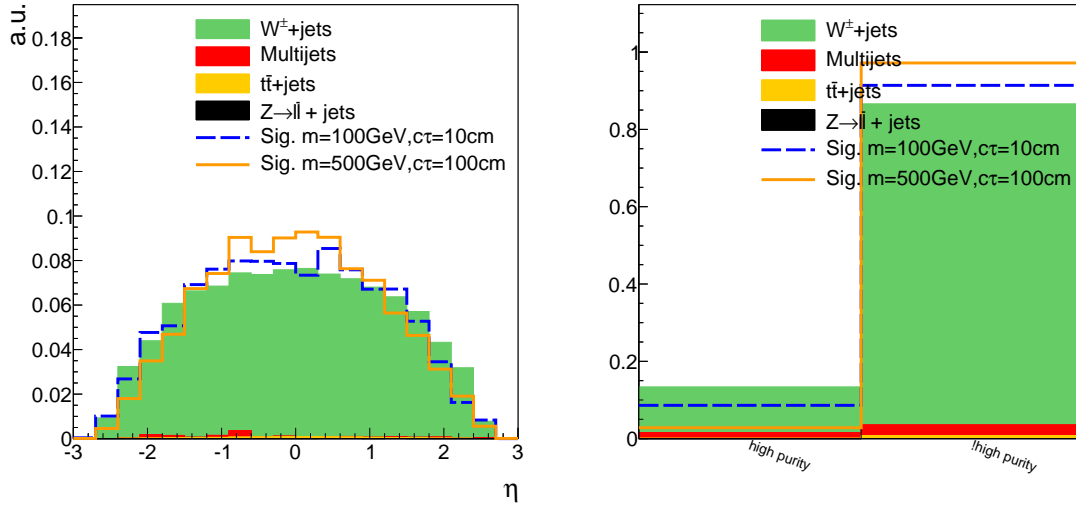


Figure 1.23: Distribution of the track's pseudorapidity (left) and the number of tracks flagged and not flagged "high-purity" (right) after trigger requirements and QCD suppression cuts.

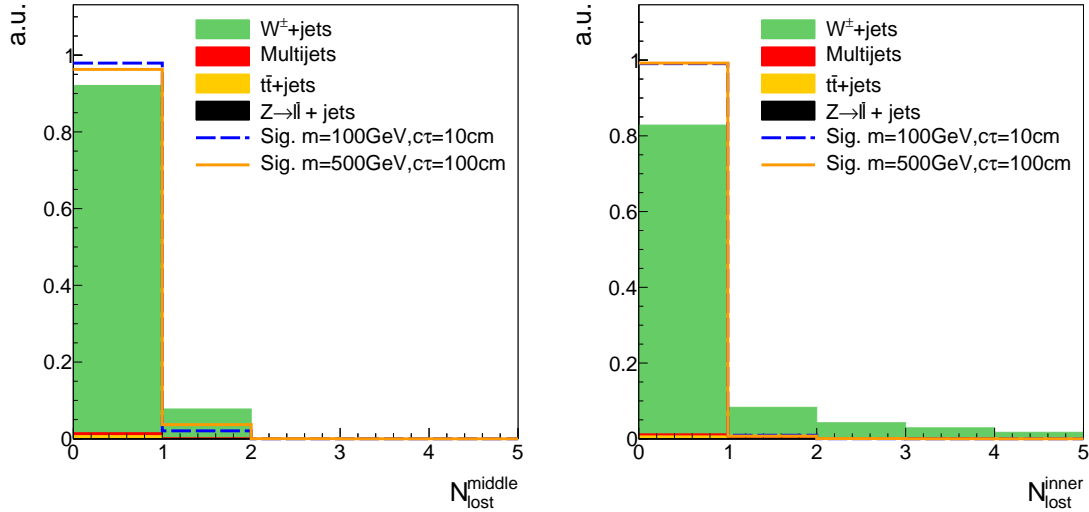


Figure 1.24: Number of missing middle (left) and inner (right) hits of background and signal tracks after trigger requirements and QCD suppression cuts.

track must not be within a cone of $\Delta R < 0.5$ around a subleading jet ($p_T < 20\text{ GeV}$ and $|\eta| < 4.5$).

Unfortunately, the lepton veto cuts lack efficiency in some of the detector directions. For example, the reconstruction of an electron easily fails in the direction of a dead ECAL cell. This reduces the discrimination power of the electron veto. For this reason, tracks which point to a dead ECAL cell within $\Delta R < 0.05$ are rejected. A general list of dead and noisy ecal cells is provided centrally at CMS. Further dead cells were identified within

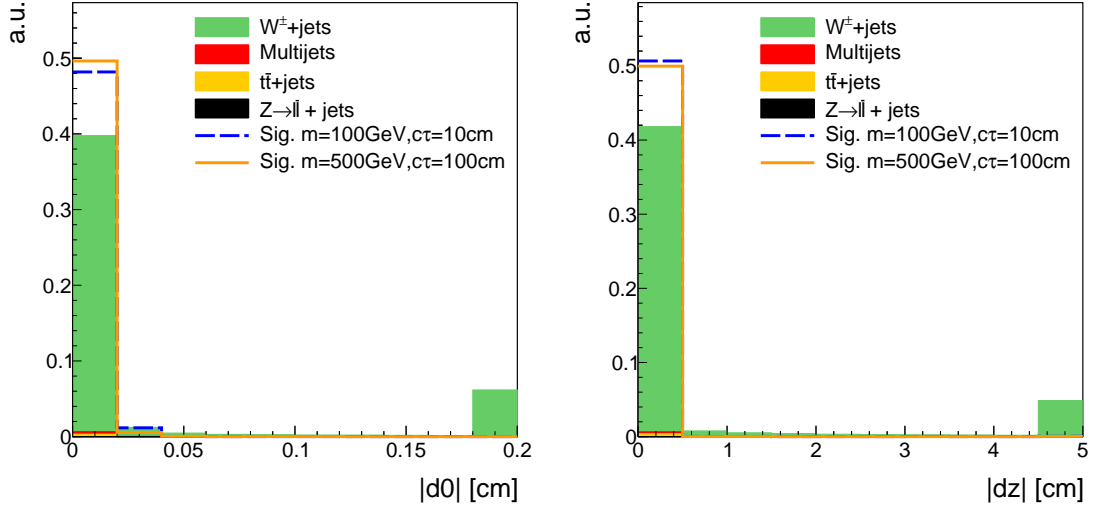


Figure 1.25: Absolute value of the radial (left) and longitudinal (right) distance between the track and the primary vertex after trigger requirements and multijet suppression cuts. Overflow entries are added to the last bin.

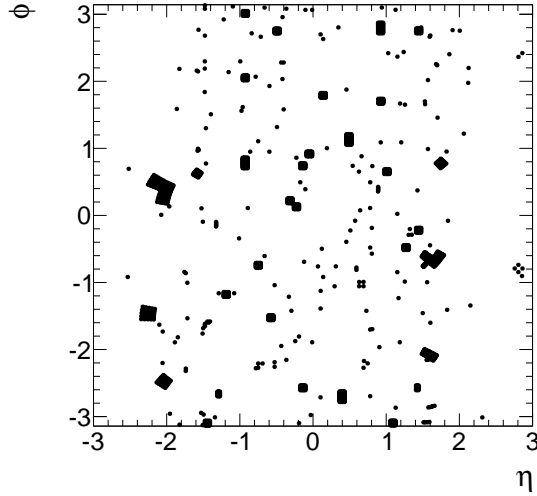


Figure 1.26: Visualization of dead and noisy ecal cells in the detector's $\phi - \eta$ plane.

a study in [7] resulting in a total number of 1234 dead or noisy ECAL channels. These are illustrated in Fig. 1.26 where a map of all ECAL channels not considered in the search is given.

Additionally, also tracks which point towards intermodule gaps of ECAL cells or to the ECAL barrel endcap gap at $1.42 < |\eta| < 1.65$ are rejected. A list of the ECAL intermodule gaps is given in Table 1.7.

The muon reconstruction is less efficient for muons in detector regions with bad cathode strip chambers (CSC). Thus, also tracks pointing in these regions within a distance of

Table 1.7: Intermodule ECAL gaps.

η -ranges
$-1.14018 < \eta < -1.1439$
$-0.791884 < \eta < -0.796051$
$-0.44356 < \eta < -0.447911$
$0.00238527 < \eta < -0.00330793$
$0.446183 < \eta < 0.441949$
$0.793955 < \eta < 0.789963$
$1.14164 < \eta < 1.13812$

$\Delta R < 0.25$ are rejected.

These considerations lead to the following selection cuts:

- ❖ The track must not be within a cone of $\Delta R < 0.15$ to a reconstructed standalone, tracker or global muon with a transverse momentum larger than 10 GeV.
- ❖ Veto all tracks within a cone of $\Delta R < 0.15$ to a reconstructed electron with a transverse momentum larger than 10 GeV.
- ❖ The track must not be within a cone of $\Delta R < 0.15$ to a reconstructed tau with $p_T > 20$ GeV and $|\eta| < 2.3$.
- ❖ No subleading jet ($p_T < 20$ GeV and $|\eta| < 4.5$) is allowed around the track in a cone of $\Delta R < 0.5$
- ❖ Veto tracks within a cone of $\Delta R < 0.05$ to a dead or noisy ECAL cell.
- ❖ The track must not point in the direction of the ECAL intermodules gap listed in Table 1.7.
- ❖ The track must not be within a cone of $\Delta R < 0.25$ to a bad CSC.
- ❖ Veto any track pointing to the region between ECAL barrel and endcap at $1.42 < |\eta| < 1.65$

Selection of candidate tracks

Finally, a last few pronounced characteristics of the chargino track are exploited. As the chargino is produced in a very clean environment, the isolation of the track (defined as the sum of all track's transverse momentum in a cone of $\Delta R < 0.3$ around the candidate track) can discriminate signal against background events. Furthermore, in case the charginos decay inside the tracker, there is no energy deposition in the calorimeters in the direction of the track. The concrete selection cuts are as follows

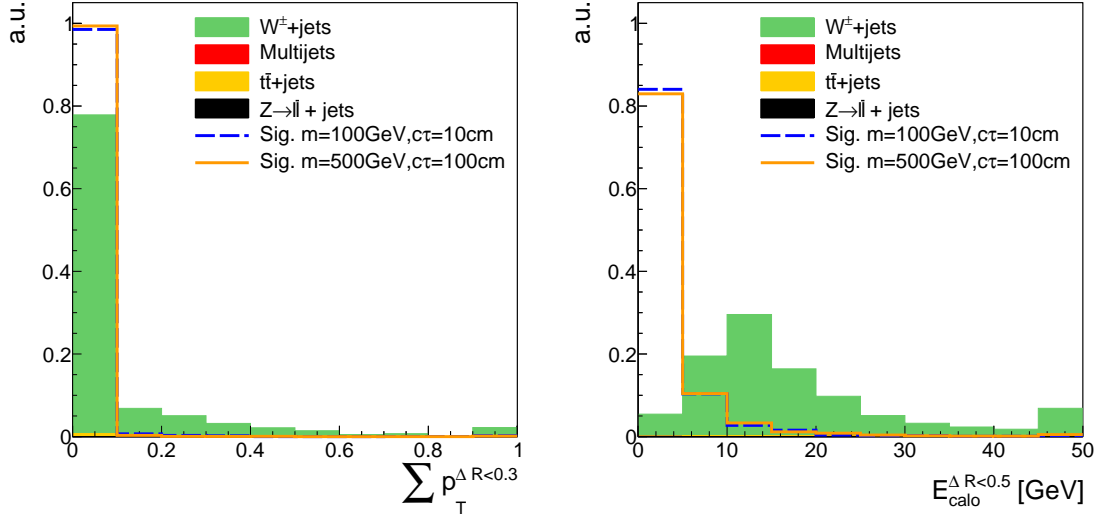


Figure 1.27: Track isolation (left) and calorimeter isolation (right) of the candidate track after the full previous selection.

- ❖ No further substantial track activity (less than 10%) is allowed in a cone of $\Delta R < 0.3$ around the candidate track: $\sum_{\Delta R < 0.3} p_T / p_T^{\text{cand}} < 0.1$
- ❖ Little calorimeter energy deposits in a cone of $\Delta R < 0.5$ around the track: $E_{\text{calo}}^{\Delta R < 0.5} < 5 \text{ GeV}$.

These two variables are shown in Fig. 1.27 after the full previous selection.

As emphasized before, this analysis aims to be as general as possible to search for charginos with different lifetimes. Although the search is designed with a focus on charginos which decay inside the tracker, no explicit selection cut is required in the number of missing outer hits. For charginos with very short mean lifetimes it was checked, whether a sensitivity increase can be achieved by imposing a cut on $N_{\text{miss}}^{\text{outer}}$. However, this is not the case and therefore a selection in $N_{\text{miss}}^{\text{outer}}$ is not considered. An illustration of the efficiency of the selection cuts for two different signal samples and simulated background is shown in Fig. 1.28. A summary of all candidate track selection criteria is given in Appendix ??.

Given the presented candidate selection requirements, a set of two variables remain, which are highly discriminating: The transverse momentum and the energy release per path length of the candidate track. In Fig. 1.30, the distribution of the remaining two variables are shown after the application of the full candidate track selection. These variables are used to optimise the sensitivity of the search in the variable $S/(S + B)$ (S =number of signal events, B =number of background events). The optimisation process will be explained in Sec ??. However, before the optimisation can be accomplished, the characterization and estimation of the background is needed. This topic will be discussed in the following section.

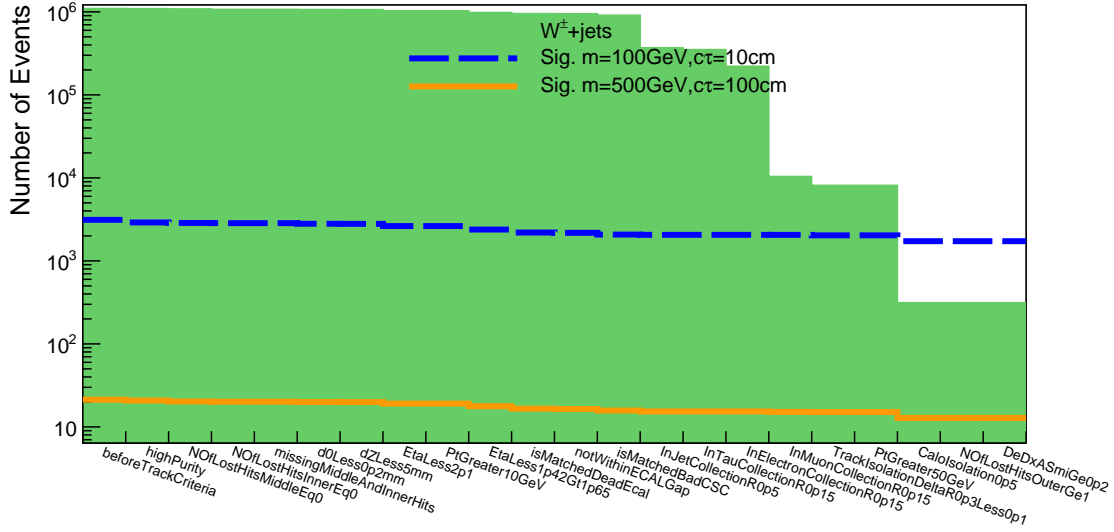


Figure 1.28: Efficiency of the analysis selection cuts for simulated signal and background samples.

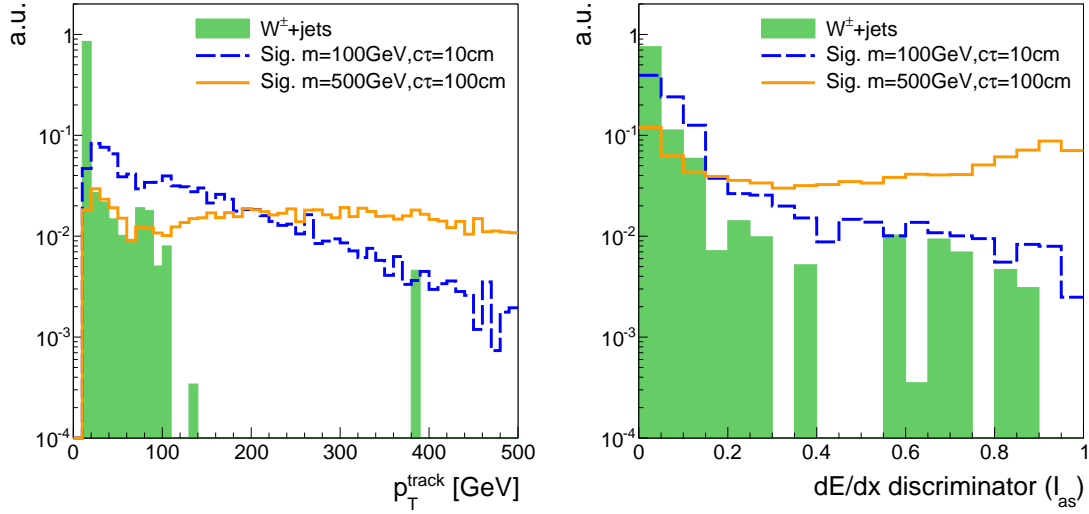


Figure 1.29: Candidate track p_T (left) and I_{as} (right) after the full candidate track selection for signal and $W + \text{jets}$ events. Because of high event weights of the $W + \text{jets}$ sample, the \cancel{E}_T and $p_T^{1,\text{jet}}$ cuts are loosen to $\cancel{E}_T > 0 \text{ GeV}$ and $p_T^{1,\text{jet}} > 70 \text{ GeV}$. As these variables are not expected to be correlated with the track characteristics it does not influences the shape of the shown distributions.

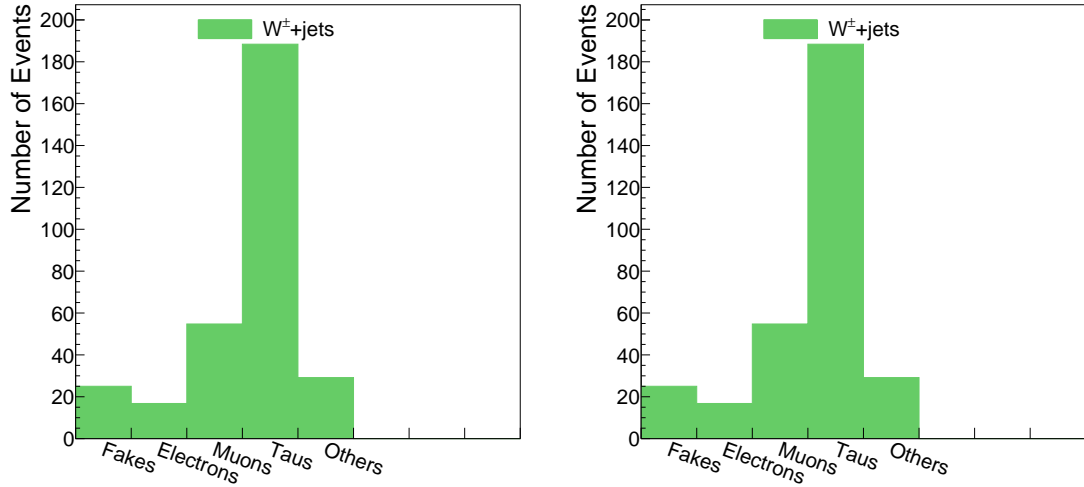


Figure 1.30: Candidate track p_T (left) and I_{as} (right) after the full candidate track selection for signal and $W + \text{jets}$ events. Because of high event weights of the $W + \text{jets}$ sample, the \cancel{E}_T and $p_T^{1,\text{jet}}$ cuts are loosen to $\cancel{E}_T > 0 \text{ GeV}$ and $p_T^{1,\text{jet}} > 70 \text{ GeV}$. As these variables are not expected to be correlated with the track characteristics it does not influences the shape of the shown distributions.

1.6 Characterisation and estimation of the Standard Model backgrounds

After the application of the candidate track selection explained in the previous section the background arising from Standard Model processes is dramatically reduced. However, it still happens sometimes that a electron, muon or tau fails reconstruction, which will be explained in detail in the following section 1.6.1. Furthermore, there is the possibility that a track is reconstructed out of a set of hits which do not origin from only one single particle. Such tracks will be called “fake tracks” in the following. Background tracks arising from wrong reconstruction will be explained in Sec. 1.6.2

The composition of the background is shown in Fig. ?? . This composition can change significantly when imposing further selection cuts on p_T and I_{as} . This, however, is addresses within the optimisation. To get a feeling how the composition can chnage, the bkg composition is shown in Fig ?? with the analysis selection plus an additional I_{as} cut of 0.5.

- Show plots with different selection cuts: after candidate track selection + $\text{ecal} < 5 \text{ GeV}$,
- Explain why we need data based approach
- Explain that we cannot know before how important the leptonic bkg is.

1.6.1 Leptonic background

The leptonic background can arise from various sources: First, ...

- Characterization - describe shortly why a background can contribute
- Electron: Explain again, that most of the preselection cuts are done for electrons
-

1.6.2 Fake background

- Show plot with fake rate in different samples

1.6.3 Systematic uncertainties

- Background consist of particles which make high energy deposits and are high pt
- In general: Low background search

1.7 Optimization of search sensitivity

- Show plots
- show table
- Include NlostOuter here, too

1.8 Statistical Methods/ Limit setting

1.9 Results

- Data cutflowtable
- Tables with results
- One plot (4 bins: Prediction and data)

1.10 Interpretation

1.10.1 Systematic uncertainties of simulated signal samples

1.10.2 Exclusion limits

- 1-d limits
- 2-d limits

Bibliography

- [1] CMS Collaboration, “Search for new physics in the multijet and missing transverse momentum final state in proton-proton collisions at $\sqrt{s}=8$ TeV”, *JHEP* **06** (2014) 055, [arXiv:1402.4770](#). doi:10.1007/JHEP06(2014)055.
- [2] CMS Collaboration, “Searches for Supersymmetry using the M_{T2} Variable in Hadronic Events Produced in pp Collisions at 8 TeV”, *JHEP* **05** (2015) 078, [arXiv:1502.04358](#). doi:10.1007/JHEP05(2015)078.
- [3] ATLAS Collaboration, “Search for squarks and gluinos with the ATLAS detector in final states with jets and missing transverse momentum using $\sqrt{s}=8$ TeV proton-proton collision data”, *JHEP* **09** (2014) 176, [arXiv:1405.7875](#). doi:10.1007/JHEP09(2014)176.
- [4] M. Ibe, S. Matsumoto, S. Shirai et al., “Wino Dark Matter in light of the AMS-02 2015 Data”, *Phys. Rev.* **D91** (2015), no. 11, 111701, [arXiv:1504.05554](#). doi:10.1103/PhysRevD.91.111701.
- [5] T. Moroi, M. Nagai, and M. Takimoto, “Non-Thermal Production of Wino Dark Matter via the Decay of Long-Lived Particles”, *JHEP* **07** (2013) 066, [arXiv:1303.0948](#). doi:10.1007/JHEP07(2013)066.
- [6] CMS Collaboration, “Searches for long-lived charged particles in pp collisions at $\sqrt{s}=7$ and 8 TeV”, *JHEP* **07** (2013) 122, [arXiv:1305.0491](#). doi:10.1007/JHEP07(2013)122.
- [7] CMS Collaboration, “Search for disappearing tracks in proton-proton collisions at $\sqrt{s}=8$ TeV”, *JHEP* **01** (2015) 096, [arXiv:1411.6006](#). doi:10.1007/JHEP01(2015)096.
- [8] CMS Collaboration, “Reinterpreting the results of the search for long-lived charged particles in the pMSSM and other BSM scenarios”, *CMS Physics Analysis Summary* **CMS-PAS-EXO-13-006** (2014).
- [9] CMS Collaboration, “Search for disappearing tracks in proton-proton collisions at $\sqrt{s}=8$ TeV”, *Public CMS Wiki* (2015). <https://twiki.cern.ch/twiki/bin/view/CMSPublic/PhysicsResultsEXO12034>, Topic revision: r9.
- [10] CMS Collaboration, “Phenomenological MSSM interpretation of the CMS 2011 5fb-1 results”, *CMS Physics Analysis Summary* **CMS-PAS-SUS-12-030** (2013).
- [11] CMS Collaboration, “Description and performance of track and primary-vertex reconstruction with the CMS tracker”, *JINST* **9** (2014), no. 10, P10009, [arXiv:1405.6569](#). doi:10.1088/1748-0221/9/10/P10009.

- [12] H. Bethe, “Theory of the Passage of Fast Corpuscular Rays Through Matter”, *Annalen Phys.* **5** (1930) 325–400. [Annalen Phys.397,325(1930)].
doi:10.1002/andp.19303970303.
- [13] “National Institute of Standards and Technology”.
<http://physics.nist.gov/cgi-bin/Star/compos.pl?mode=text&matno=014>.
Accessed: 2015-10-21.
- [14] Particle Data Group Collaboration, “Review of Particle Physics”, *Chin. Phys.* **C38** (2014) 090001. doi:10.1088/1674-1137/38/9/090001.
- [15] L. Landau, “On the energy loss of fast particles by ionization”, *J. Phys.(USSR)* **8** (1944) 201–205.
- [16] H. Bichsel, “Straggling in Thin Silicon Detectors”, *Rev. Mod. Phys.* **60** (1988) 663–699. doi:10.1103/RevModPhys.60.663.
- [17] L. Quertenmont, “Search for Heavy Stable Charged Particles with the CMS detector at the LHC”. PhD thesis, Louvain, U., 2010.
- [18] T. W. Anderson, “On the Distribution of the Two-Sample Cramr-von Mises Criterion”, *The Annals of Mathematical Statistics* **33** (1962), no. 3, pp. 1148–1159.
- [19] F. James, “Statistical methods in experimental physics”. 2006.
- [20] CMS Collaboration, “Tracking and Vertexing Results from First Collisions”, *CMS Physics Analysis Summary CMS-PAS-TRK-10-001* (2010).
- [21] R. Gavin et al., “FEWZ 3.1: A User’s Guide”.
http://www.hep.anl.gov/fpetriello/FEWZManual_3.1.pdf. Accessed:
2015-10-27.
- [22] M. Czakon, P. Fiedler, and A. Mitov, “Total Top-Quark Pair-Production Cross Section at Hadron Colliders Through $O(\frac{4}{S})$ ”, *Phys. Rev. Lett.* **110** (2013) 252004, arXiv:1303.6254. doi:10.1103/PhysRevLett.110.252004.
- [23] J. Alwall, R. Frederix, S. Frixione et al., “The automated computation of tree-level and next-to-leading order differential cross sections, and their matching to parton shower simulations”, *JHEP* **07** (2014) 079, arXiv:1405.0301.
doi:10.1007/JHEP07(2014)079.
- [24] T. Sjostrand, S. Mrenna, and P. Z. Skands, “PYTHIA 6.4 Physics and Manual”, *JHEP* **05** (2006) 026, arXiv:hep-ph/0603175.
doi:10.1088/1126-6708/2006/05/026.
- [25] GEANT4 Collaboration, “GEANT4: A Simulation toolkit”, *Nucl. Instrum. Meth.* **A506** (2003) 250–303. doi:10.1016/S0168-9002(03)01368-8.
- [26] J. Allison et al., “Geant4 developments and applications”, *IEEE Trans. Nucl. Sci.* **53** (2006) 270. doi:10.1109/TNS.2006.869826.

- [27] B. Fuks, M. Klasen, D. R. Lamprea et al., “Gaugino production in proton-proton collisions at a center-of-mass energy of 8 TeV”, *JHEP* **1210** (2012) 081, [arXiv:1207.2159](#). doi:10.1007/JHEP10(2012)081.
- [28] B. Fuks, M. Klasen, D. R. Lamprea et al., “Precision predictions for electroweak superpartner production at hadron colliders with Resummino”, *Eur.Phys.J.* **C73** (2013) 2480, [arXiv:1304.0790](#). doi:10.1140/epjc/s10052-013-2480-0.
- [29] CMS Collaboration, “Tracking and Primary Vertex Results in First 7 TeV Collisions”, *CMS Physics Analysis Summary* **CMS-PAS-TRK-10-005** (2010).
- [30] A. B. et. al., “Search for New Physics in the Monojet final state at CMS”, *CMS Analysis Note* **CMS-AN-12-421** (2012). Internal documentation.
- [31] CMS Collaboration, “Search for dark matter, extra dimensions, and unparticles in monojet events in protonproton collisions at $\sqrt{s} = 8$ TeV”, *Eur. Phys. J.* **C75** (2015), no. 5, 235, [arXiv:1408.3583](#). doi:10.1140/epjc/s10052-015-3451-4.

